Density measurements in free jets from axisymmetric supersonic nozzles with constant-area straight ducts

Author(s):
Awata, Y.; Nakao, S.; Miyazato, Y.

Publication date:
2018-10-05

Permanent link:
https://doi.org/10.3929/ethz-b-000279218

DENSITY MEASUREMENTS IN FREE JETS FROM AXISYMMETRIC SUPERSONIC NOZZLES WITH CONSTANT-AREA STRAIGHT DUCTS

Y.Awata[1], S.Nakao[1], and Y. Miyazato[1,c]

[1] Department of Mechanical Systems Engineering, The University of Kitakyushu, 1-1 Hibikino, Wakamatsu-ku, Kitakyushu, Fukuoka, 808-0135, Japan
[c]Corresponding author: Tel.: +81936953219; Email: miyazato@kitakyu-u.ac.jp

KEYWORDS:
Main subjects: density measurement, flow visualization
Fluid: supersonic flows
Visualization method(s): rainbow schlieren deflectometry
Other keywords: computed tomography, Abel inversion

ABSTRACT: *The free jet issued from a supersonic nozzle with a design Mach number of 1.5 followed by a constant area straight duct with an inner diameter of 10 mm has been investigated experimentally and numerically under a slightly underexpanded condition. Quantitative flow visualization has been performed using the rainbow schlieren deflectometry combined with the computed tomography. Three-dimensional jet density fields for the experiment are obtained by the Abel inversion and computed tomography algorithms. The numerical simulation was carried out using the RANS equations with Menter's* SST*k-w turbulent model for a mutual comparison with the experiment. The fine structure of the free-jet is demonstrated with density contour plots including the jet centerline, streamwise and radial density profiles.*

1 Introduction

To understanding the prominent characteristics of complex shock-containing flows, schlieren and shadowgraph methods [1] are widely used as optical tools because of its simple optical arrangement with a high degree of resolution and ability to observe easily such structures as shock waves, Prandtl-Meyer compression and expansion waves in supersonic flows. However, conventional schlieren techniques have been extensively employed for qualitative flow visualization because they take considerable effort to extract quantitative properties. Another simplest method for visualizing jet flow fields with varying refractive index quantitatively is probably the rainbow schlieren deflectometry [2]. This technique is a modified form of basic color schlieren and the color filter in the schlieren cutoff plane is only replaced by a rainbow filter with continuous color stripe distribution. Kolhe and Agrawal [3] measured the flow characteristics of the shock-containing jet issued from an axisymmetric cylindrical nozzle by the rainbow schlieren deflectometry. Takano et al. [4] have performed three-dimensional density measurements in an underexpanded sonic jet with a Mach disk from a round convergent nozzle with an exit diameter of 10 mm and demonstrated that the rainbow schlieren combined with the computed tomography can be effectively used for quantitative measurements of density in asymmetric shock-containing jets. However, experimental data with high accuracy and reliability on shock-containing free jets are still lacking in the current literature. Therefore, in the present study, for obtaining quantitative experimental data with high precision as well as high spatial resolution for shock-containing free jets, the rainbow schlieren deflectometry is applied for slightly underexpanded jets from an axisymmetric supersonic nozzle followed by a constant-area straight duct.

Such long supersonic nozzles attract special attentions on applications to the high velocity oxygen fuel (HVOF) coating technology, gas-burner system, and cold spray technology [5] . Density fields in free jets are reconstructed by two methods. One is the so-called Abel inversion algorithm and the other is the rainbow schlieren deflectometry combined with the computed tomography based upon the convolution back-projection algorithm. In addition to the experimental work, the free jet under the same conditions as that in the experiment is solved using the RANS equations with the SSTk-ω turbulent model. A quantitative comparison between experiment and simulation is carried out to investigate three-dimensional spatial variations of the free jet.

2 Experimental apparatus

A schematic drawing of experimental apparatus is shown in Fig. 1. Experiments have been performed in a blow-down supersonic wind tunnel with the jet issued in the quiescent laboratory air. The test nozzle used in the present experiment is shown in Fig. 2. The test nozzle consists of an axisymmetric supersonic nozzle with a design Mach number of 1.5 followed by a constant area straight duct with an inner diameter of 10 mm. The wall contours of the supersonic nozzle are designed by the axisymmetric method of characteristics [6] to provide parallel and uniform flow at the nozzle exit. The air supplied by a compressor that pressurizes the ambient air up to 1 MPa is filtered, dried and stored in a high-pressure reservoir consisting of two tanks with a total capacity of 2 m^3. The high-pressure dry air from the reservoir is stagnated in a plenum chamber and then discharged into the atmosphere through the test nozzle. The total temperature in the plenum chamber is equal to the room temperature, and the plenum pressure is controlled and maintained constant during the testing by a valve. The jet issued from the nozzle is visualized by the rainbow schlieren deflectometry for a nozzle pressure ratio of 4.0. The rainbow schlieren system consists of rail-mounted optical components including a 3 mm × 50 μm rectangular pinhole, two 100 mm diameter, 500 mm focal length achromatic lenses, a computer generated 23 mm wide slide with color gradation in a 2.0 mm wide strip, and a digital camera (Nikon D7100) with a 30 mm diameter focusing lens of 600 mm focal length. A continuous 250 W metal halide light source connected to a 50 μm diameter fiber optic cable provides the light input at the pinhole through a 16.56 mm focal length objective lens. The camera output in the RGB format is digitized by a personal computer with 24 bit color frame grabber. Multiple viewing rainbow schlieren pictures are acquired over a range of nozzle angular angles from 0 deg to 180 deg by rotating the nozzle about its longitudinal axis (z axis) in equal angular intervals of 10 deg and the jet three-dimensional density field is reconstructed using the convolution back-projection algorithm.

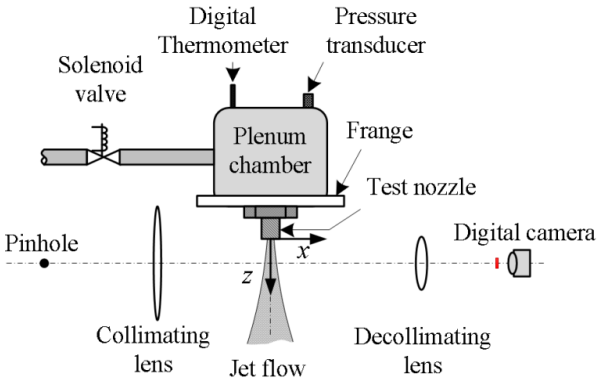

Fig.1. Schematic of experimental apparatus

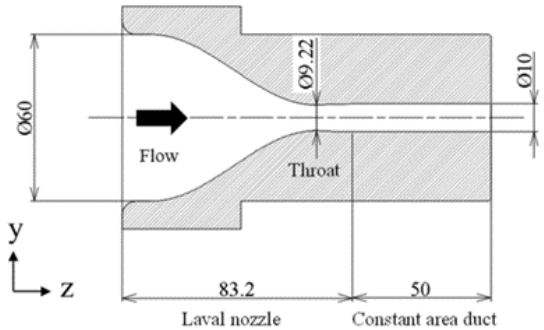

Fig. 2. Test nozzle

3 Principle of tomographic rainbow schlieren

3.1 Abel inversion method

Light rays passing through the refractive index field are bent by refraction and have an angle of inclination with respect to their original path. Figure 3 shows a parallel incident light ray interacting with an axisymmetric flow where the flow direction is from the negative to positive z axes in an x,y,z – rectangular Cartesian coordinate system. For light rays passing through an axisymmetric flow field, the refractive index n in the flow field depends only on the radial distance r from the origin O ($x = y = 0$) as shown in Fig. 3, i.e.,

$$n = n(r), \quad for \quad 0 \le r \le R, \quad n = n_a, \quad for \quad R < r \tag{1}$$

where n_a is the refractive index of surrounding air.

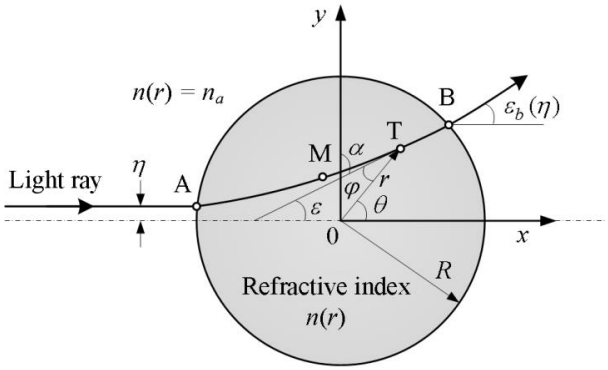

Fig. 3. Light ray travelling through axisymmetric refractive index field

Consider the variation of the collimating light ray entering parallel to the x axis as shown in Fig. 3. The light ray at the normal distance $y = \eta$ from the x axis at Point A is assumed to leave Point B with a deflection angle $\varepsilon_b(\eta)$ after passing through the refractive index field.

Let T = T(r,θ) be an arbitrary location on a light ray in the field with the polar coordinate system, the angle α between the y axis and the tangent line of the ray at the Point T, and the angle φ between the tangent line and the position vector **OT** are expressed, respectively, as follows:

$$\tan\alpha = \frac{\dfrac{dr}{d\theta} - r\tan\theta}{\tan\theta\dfrac{dr}{d\theta} + r} \tag{2}$$

$$\tan\varphi = -\frac{r}{\dfrac{dr}{d\theta}} \tag{3}$$

Using the theory of the light-ray traces through a medium with axial symmetry, the following relation can be derived [7]

$$nr\sin\varphi = \text{const.} \tag{4}$$

If the point on the ray for the φ corresponding to a right angle is given as Point M = M(r_m, θ_m) for $0 \le \theta \le \theta_m$ $\left(0 \le \varphi \le \pi/2\right)$, and using Eq. (4),

$$\sin\varphi = \frac{\psi}{nr} \tag{5}$$

$$\cos\varphi = \frac{\sqrt{(nr)^2 - \psi^2}}{nr} \tag{6}$$

Differentiation of Eq. (5) and rearrangement with Eq. (6) leads to

$$d\varphi = -\frac{\psi\left(rdn + ndr\right)}{nr\sqrt{(nr)^2 - \psi^2}} \tag{7}$$

Combination of Eqs. (3), (5), and (6) leads to

$$d\theta = -\frac{\psi dr}{r\sqrt{(nr)^2 - \psi^2}} \tag{8}$$

As shown in Fig. 3, if ε is the angle between the tangent line of the ray at T and x axis, $\varepsilon = \theta - \varphi$, therefore, the derivative gives

$$d\varepsilon = d\theta - d\varphi \tag{9}$$

From Eq. (7) ~ (9), it follows that

$$d\varepsilon = \frac{\psi dn}{n\sqrt{(nr)^2 - \psi^2}} \tag{10}$$

where since $r\sin\varphi$ physically means that the vertical distance from the origin O to the tangent line of the ray at Point T, it follows that $r\sin\varphi = \eta$ with $n = n_a$ for $\theta = \pi$ and $r \to \infty$. From this result and Eq. (4),

$$\psi = n_a\eta \tag{11}$$

Substitution of Eq. (11) into Eq. (10) and retaining only the lowest order terms with taking account of $0 < n - 1 \ll 1$ and $0 < n_a - 1 \ll 1$, it follows that

$$d\varepsilon = \frac{\eta \dfrac{dn}{dr}}{n\sqrt{r^2 - \eta^2}} dr \tag{12}$$

Next, if the angles between each tangent line at Points A and M on the ray and *x* axis are given as $\varepsilon_a(\eta)(= 0)$ and $\varepsilon_m(\eta)$, respectively, from the geometric symmetry with respect to Point M on the light ray travelling from Points A to B, it follows that $\varepsilon_m(\eta) - \varepsilon_a(\eta) = \varepsilon_b(\eta) - \varepsilon_m(\eta)$, therefore,

$$\varepsilon_b(\eta) = 2\int_{\varepsilon_m(\eta)}^{\varepsilon_b(\eta)} d\varepsilon \tag{13}$$

where if $\varepsilon = \varepsilon_m(\eta)$ at $r = r_m$ and $\varepsilon = \varepsilon_b(\eta)$ at $r = R$, from Eq. (12) and (13), it follows that

$$\varepsilon_b(\eta) = 2\eta\int_{r_m}^{R} \frac{\dfrac{dn}{dr}}{\sqrt{r^2 - \eta^2}} dr \tag{14}$$

An assumption of $\left|\varepsilon_m(\eta)\right| \ll 1$ gives $r_m \doteq \eta / \cos\left[\varepsilon_m(\eta)\right] \doteq \eta$ and since $dn/dr = 0$ for $R \le r$, Eq. (14) reduces to [2].

$$\varepsilon_b(\eta) = 2\eta\int_{\eta}^{\infty} \frac{\dfrac{dn}{dr}}{\sqrt{r^2 - \eta^2}} dr \tag{15}$$

The ray deflection angle is transformed by the decollimating lens to transverse displacement at the cut-off plane given by

$$d(\eta) \cong \varepsilon_b(\eta) f_d \tag{16}$$

where f_d is the focal length of the decollimating lens.
The ray displacement can be found from the calibration curve between hue and transverse displacement at the filter plane as stated in the next section. Once the angular ray deflections are calculated from Eq. (4), the refractive index field is found by inverting Eq. (15) using the Abel inversion.

$$n(r) = n_a - \frac{1}{\pi}\int_{r}^{\infty} \frac{\varepsilon(\eta) d\eta}{\sqrt{\eta^2 - r^2}} \tag{17}$$

The refractive index $n(r)$ is a function of density ρ and Gladstone-Dale constant K. The relation between $n(r)$ and ρ is approximately linear and is usually written as:

$$n(r) = 1 + K\rho(r) \tag{18}$$

As the K hardly depends on the wavelength of light, the same constant is used for all wavelengths [2].

3.2 Schlieren CT method

The problem of obtaining reliable quantitative information about the flow structure of three-dimensional supersonic jets arises in many industrial fields. Although direct imaging such as the conventional schlieren cannot provide quantitative information about the structure of three dimensional jets, the schlieren CT which combines the rainbow schlieren deflectometry with so-called computed tomography, often abbreviated as CT must be utilized. Computed tomography was originally developed for use in medical diagnostics with X-rays, but was later adapted for other applications in many scientific fields including physics, chemistry, astronomy, and geophysics, using in many cases other kinds of radiation and even elementary particles. Various CT reconstruction algorithms including the Fast Fourier transform (FFT) algorithm, the filter back projection (FBP) algorithm, and the convolution-back projection (CBP) algorithm have been provided so far. Among them the present study adopts the CBP algorithm because it performs best when data are available at all viewing angles [8, 9]. A brief outline of computed tomography for density fields in the three-dimensional jet flows is given by Agrawal et al. [8] and Faris et al. [10].

Figure 4 shows a light ray traveling in a cross-section (x, y plane) of an asymmetric jet issued from a nozzle where the x, y, z rectangular Cartesian coordinate system is used and the z axis is perpendicular to the x, y plane which includes the vector along the optical axis direction of the schlieren system. Also, the n and n_a in Fig. 4 indicate the refractive index in the jet cross-section and that of the surrounding air, respectively. The refractive index or density fields will now be investigated for a cross section of z = constant.

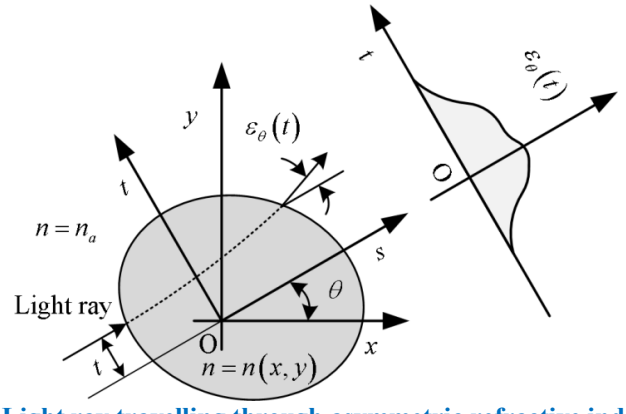

Fig. 4. Light ray travelling through asymmetric refractive index field

As shown in Fig. 4, let us consider the rotated coordinates (s, t) inclined at an angle θ away from the fixed-original coordinates (x, y). Then, a light ray traveling in the s direction with an offset of t from the axis s is bent by the interaction with the jet flow and has an angle of inclination $\varepsilon_\theta(t)$ with respect to its original path. As the incoming ray is initially parallel to the s axis, the deflection angle $\varepsilon_\theta(t)$ after passing through the refractive index field is given by the line integral

$$\varepsilon_\theta(t) = \int_{-\infty}^{\infty} \frac{\partial \eta(s,t)}{\partial t} ds \tag{19}$$

along the s direction of the partial derivative $\partial\eta/\partial t$ with respect to the t variable of the normalized refractive index difference

$$\eta(s,t) \equiv \frac{n - n_a}{n_a} \tag{20}$$

for small ray deflections. The deflection angle $\varepsilon_\theta(t)$ is taken for a range of various angles from $\theta = 0$ deg to 180 deg. The task of tomographic reconstruction in the present investigation is to find $\eta(x,y)$ based upon a given knowledge of $\varepsilon_\theta(t)$ and then density fields can be obtained through a well-known linear relation between refractive index and density, as described later.
After the one-dimensional Fourier transform of Eq. (19) with respect to the t variable and using the Leibniz rule for differentiation under the integral sign, it reduces to a relation,

$$\int_{-\infty}^{\infty} \varepsilon_\theta(t) \exp(-i2\pi t\zeta)\, dt = 2\pi i\zeta \int_{-\infty}^{\infty}\int_{-\infty}^{\infty} \eta(s,t) \exp(-i2\pi t\zeta)\, ds dt \tag{21}$$

The transformation from the (s,t)-coordinate to (x,y)-coordinate for the integral of the right-hand side of Eq. (21) yields the following form with $u = -\zeta\sin\theta$ and $\upsilon = \zeta\cos\theta$

$$\int_{-\infty}^{\infty}\int_{-\infty}^{\infty} \eta(s,t) \exp(-i2\pi t\zeta)\, ds dt = \int_{-\infty}^{\infty}\int_{-\infty}^{\infty} \eta(x,y) \exp\left[-i2\pi(ux + \upsilon y)\right] dx dy \tag{22}$$

This equation expresses the two-dimensional Fourier transform of $\eta(x,y)$. Hence, the inverse Fourier transform of Eq. (21) using the result of Eq. (22) with the convolution theorem leads to

$$\eta(x,y) = \int_0^{\pi} \left[\varepsilon_\theta(t) * k(t)\right]_{t=-x\sin\theta + y\cos\theta} d\theta \tag{23}$$

where $k(t)$ is given by Agrawal et al. [8]

$$k(t) = \frac{\sin^2(\pi t f_{\max})}{\pi^2 t} \tag{24}$$

with the Nyquist frequency $f_{\max}$ and the symbol * denotes convolution between $\varepsilon_\theta(t)$ and $k(t)$.

When deflection data are sampled at a spacing of Δt, only frequencies below the Nyquist frequency

$$f_{\max} = \frac{1}{2\Delta t} \tag{25}$$

are adequately sampled.
The ray deflection angle $\varepsilon_\theta(t)$ is correlated with the focal length f_d of a decollimating lens and the ray transverse displacement $d_\theta(t)$ at the cut-off plane of the schlieren system and given by

$$\varepsilon_\theta(t) = \frac{d_\theta(t)}{f_d} \tag{26}$$

For air there is a simple linear relation between the refractive index $n(x,y)n$ and the gas density $\rho(x,y)$:

$$\rho(x,y) = \frac{n(x,y)-1}{K} \tag{27}$$

These two-dimensional density fields could be stacked together to form the three dimensional density field of the jet plume.

4 Numerical methods

The jet flow issued from an axisymmetric laval nozzle with an inner diameter of 10 mm at the nozzle exit was calculated using the commercial CFD software ANSYS Fluent Version 15.0. Figure 5(a) shows a schematic drawing of the computational domain and coordinate system for the present numerical simulation. The center on the nozzle exit plane is taken as the origin. The z and r axes are the downstream distance and radial distance from the origin, respectively and D_e the inner diameter of the nozzle exit. The present flow is assumed to be symmetric with respect to the z axis, therefore, only the upper half of the domain needs to be considered. The axisymmetric Reynolds-averaged Navier-Stokes (RANS) equation is numerically solved. In the present simulation, a turbulent model is utilized to close the governing equation because the Reynolds number for the present experiment is 6.16 x 10^4 and the experimental results by Nakao and Takamoto [11] on the choking flows through critical nozzles including Laval-typed and convergent-typed nozzles show that a boundary layer transition from laminar to turbulent flow occurs at a throat Reynolds number of around 10,000. In the past, although various turbulent models have been proposed, the well-known Menter's *SSTk-ω* turbulent model is employed in the present study because it is extensively used in many mechanical, industrial and aerospace CFD applications such as flows in intakes, nozzles, diffusers and channels, transonic and supersonic flows, shock-wave-boundary layer interactions [12].
The inlet and ambient conditions are identical to the experimental ones where the plenum pressure and temperature upstream of the nozzle are held constant at 404 kPa and 300 K, respectively, and the back pressure is set at the atmospheric pressure 101 kPa. Therefore, the nozzle operating pressure ratio defined as the ratio p_{os}/p_b of the plenum pressure p_{os} to back pressure p_b is kept constant at 4.0. The dry air is assumed to obey the perfect gas law with a constant specific heat ratio of γ = 1.4, and the

coefficient of viscosity is assumed to vary according to the Sutherland's formula. Figures 5(b) and 5(c) indicate an image of computational mesh and a zoom view of the mesh near the nozzle exit, respectively. The boundary conditions are the adiabatic no-slip on the nozzle walls, and the upstream and downstream ends of the computational domain are taken as free boundaries. The flow domain is discretized using approximately 300,000 structured elements. The grid spacing in the z direction is made small within the region from $z = 0$ to $7D_e$. Inside the nozzle, the grid size smoothly decreases in the radial direction to capture the boundary layer. To capture precisely the fine structure of shock-containing free jet, a minimum mesh interval of around 6 μm is used in the areas inside the nozzle and downstream of the nozzle. The computations are performed using structured grids. The number of iterations is 5,000, which is sufficient to guarantee that the governing equations can be accurately solved. The CFL number is 0.1 for the present simulation. The physical values on the left and right sides of the cell boundary are calculated by the MUSCL approach with the differentiable limiter. This scheme satisfies a total-variation-diminishing (TVD) condition and has third-order accuracy in space. The viscous flux is determined by a second order central difference scheme. The time integration is performed by the three-stage Runge-Kutta method.

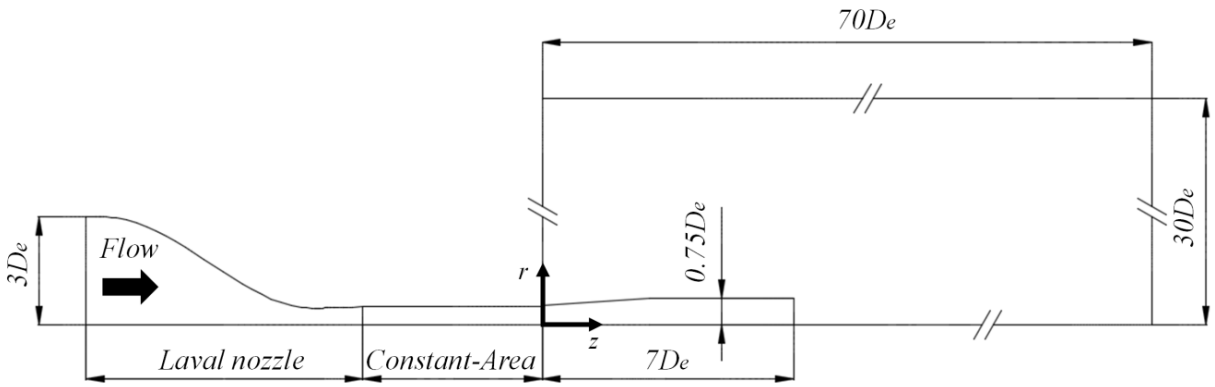

(a) Computational domain

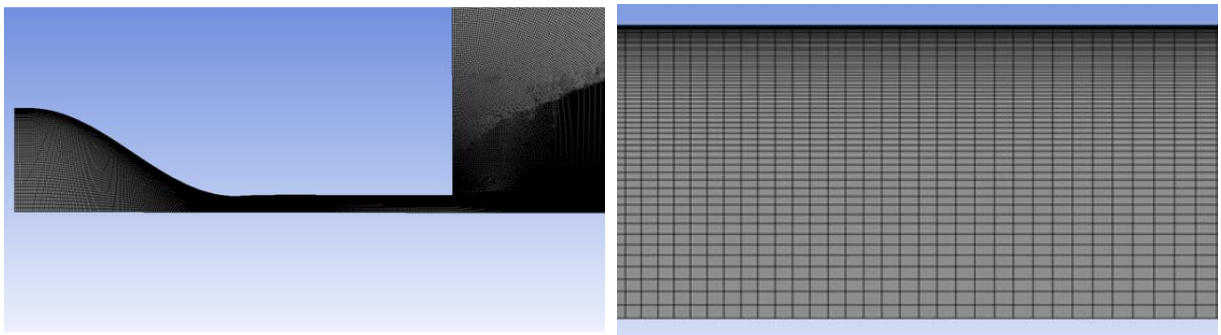

(b) Image of computational mesh **(c) Zoom of mesh in nozzle**

Fig. 5. Schematic of computational domain and image of computational mesh

5 Results and Discussion

A free jet issued from a Mach 1.5 supersonic nozzle followed by a constant-area straight duct is visualized using a rainbow schlieren system for a nozzle operating condition of $p_{os}/p_b = 4.0$ where p_{os} is the plenum pressure and p_b is the back pressure or atmospheric pressure. Schlieren picture is taken using a shutter speed of 8 kHz with continuous schlieren light source. Also, the rainbow filter is placed at the cut-off plane in parallel with respect to the z axis and its orientation is illustrated above Fig. 6 with the location of the background hue represented as the dashed line on the filter. Figure 6 exhibits a typical shock-cell pattern repeating expansion and compression toward the downstream direction from the nozzle exit. Also, the jet consists of three-shock cells with the structure symmetrical with respect to the jet centerline.

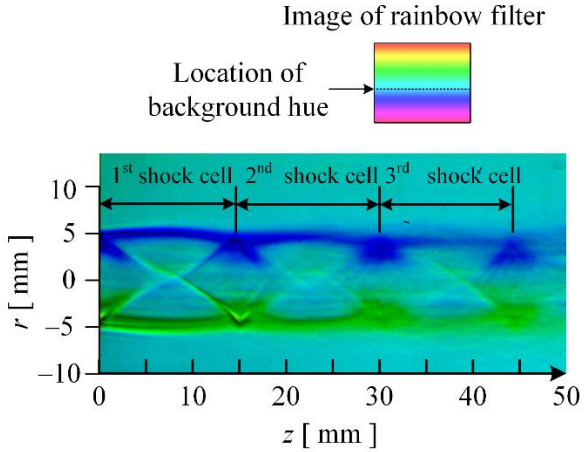

Fig. 6. Rainbow schlieren picture

Comparisons between experiment and simulation for the density contour plot on a cross-section including the jet centerline, are depicted in Figs. 7(a) ~7(c). The contour levels with an interval of 0.1 kg/m^3 are shown at the top, and the spatial resolution in the experimental density map is around 13 μm. The schlieren picture can only provide integrated information about the density gradient along in the direction of the optical axis, however, Figs. 7(a) ~ 7(c) can clearly demonstrate the quantitative information of the density field in three-dimensional jet plume. Unlike the schlieren pictures of Fig. 6, the density contour plots shown in Fig. 7 illustrate the various flow features of the shock cell structures quantitatively, such as the shape and size of the expansion and compression regions, shock cell intervals, jet boundaries and so on.

Figures 7(a) and 7(b) indicate density contour plots obtained from the experiment and they are reconstructed using the Abel inversion and the computed tomography, respectively, and Fig. 7(c) is the simulated density contour plot. The density contour plots from both the experiments are in good quantitative agreement with each other. Good quantitative agreement is reached on the sizes and shapes of expansion and compression regions in the jet plume and their streamwise locations, and the fine-structure of density fields in the shock-cell. On the other hand, the simulation is identical with both the experiments in the sizes of the expansion and compression regions and shock-cell lengths, however, it cannot capture the fine-structure of the density fields in the jet plume.

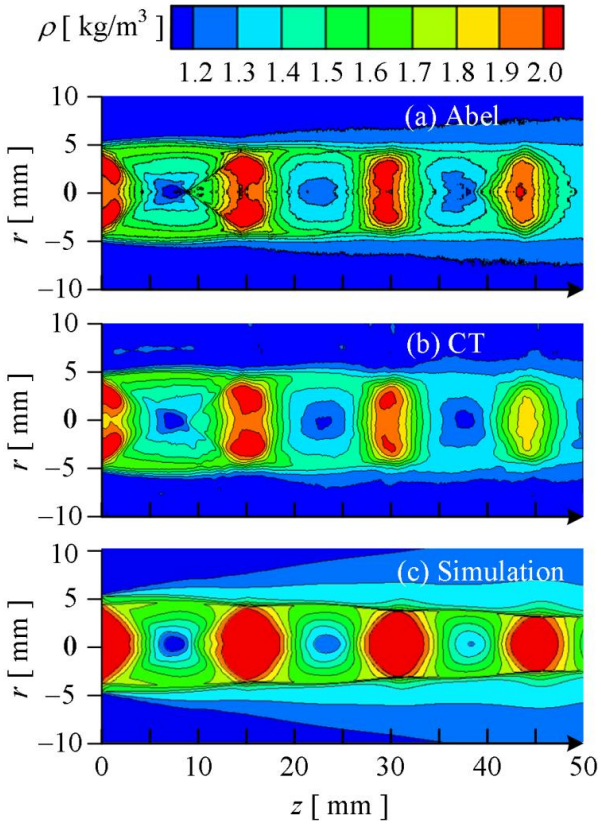

Fig. 7. Density contour plots including jet centerline

A comparison between experiment and simulation for the density profile along the jet centerline is shown in Fig. 8. The theoretical density estimated based upon the assumption of the one-dimensional isentropic flow from the inlet of the nozzle to the exit is shown as a leftward arrow on the vertical axis in Fig. 8. In addition, the fully expanded jet density ρ_j is calculated from the definition that the flow of the nozzle inlet is isentropically expanded to the back pressure and its density level is shown as the solid line parallel to the abscissa. In this regard, it is necessary to keep in mind that the fully expanded jet pressure p_j is identical with the back pressure p_b, but the ρ_j is not equal to the ambient density ρ_b.
Let us focus on the experimental density profile obtained using the Abel inversion method in Fig. 8 for the moment. Since the static pressure at the nozzle exit plane is greater than the back pressure on the present nozzle operating condition (p_{os}/p_b = 4.0), Prandtl-Meyer expansion waves are produced from the lip of the nozzle exit. Since the nozzle pressure ratio is only slightly larger than the design condition (a nozzle pressure ratio of 3.67) for the present nozzle, the expansion waves from the nozzle lip are not merged into an intercepting shock wave after reflected as compression waves at the opposite jet boundary, i.e., the inviscid wave reflection between the jet opposite boundaries seems to be repeated toward the downstream direction to some extent. As a result, the density profile has the structure similar to a sinusoidal wave except for some minor oscillations on the profile. The density profile from the CT algorithm is almost the same as that from the Abel algorithm. Streamwise distances of the local maxima and minima on the density profiles and the density values at their locations agree extremely well. The exception is differences between density values at the local maximum of z = around 44 mm and the density profile from the Abel algorithm contain minor oscillations on the profile, but that from

the CT algorithm does not. The simulated density also decreases gradually with increasing streamwise distance by the expansion waves from the nozzle lip till entering the compression region in the first shock-cell, and then raise and fall in density is repeated in the downstream direction. However, the density values at the local maxima on the density profile are higher in the simulation than in the experimental ones, while for the streamwise locations of the local maxima, there is good agreement between the simulation and experimental ones.

Comparisons between experiment and simulation for radial density profiles at a streamwise distance of z = 7 mm are depicted in Figs. 9. These profiles indicate the density variation in the middle of the first shock-cell. The simulated density profile has two distinct local maxima (shown as the leftward arrow) and one local minimum at the center axis (r = 0). The density values at the local maxima are identical with the ρ_j, and their radial locations nominally correspond to the inviscid jet boundaries [13]. The static pressures become equal to back pressure outside the inviscid boundaries. The densities at the inviscid jet boundaries gradually decrease through the jet shear layers to the ambient density.The density profiles for the experiments are nearly the same trend as the simulation, and excellent agreement is reached between both the experiments except for the outside the jet boundaries.

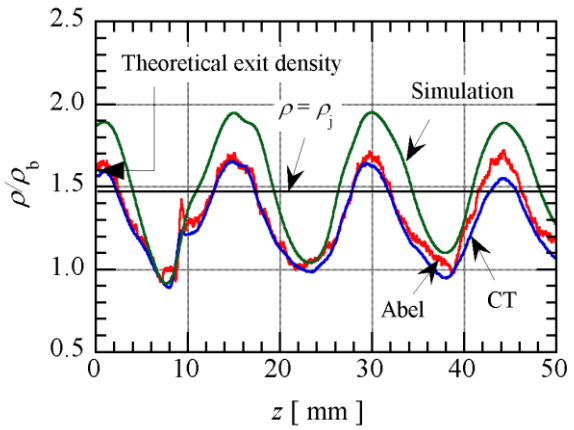

Fig. 8. Comparison of centerline density profiles

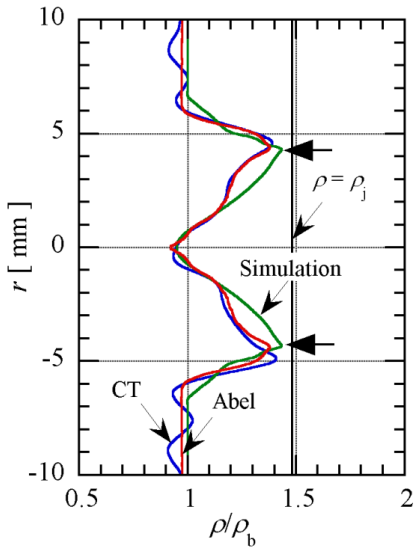

Fig. 9. Comparison of radial density profiles

6 Concluding Remarks

The density field in an underexpanded sonic jet issued from an axisymmetric supersonic nozzle followed by a constant area straight duct was quantitatively obtained by the rainbow schlieren deflectometry where the density fields were reconstructed by the Abel inversion and convolution back-projection algorithms. Also, the free jet under the same conditions as in the experiment was solved using the RANS equations with the k-ωSST turbulent model for a mutual comparison between experiment and simulation. As a result, a distinct spatial variation of the jet structure for long supersonic nozzles was clarified. It is found that the rainbow schlieren deflectometry is a very efficient tool to validate numerical simulation codes.

7 References

[1] Settles, G.S., Numerical methods for reducing line and surface probe data, SIAM Review, 2-3, pp. 200-207, 1960.

[2] Al-Ammer, K., Agrawal, K., Gollahalli, S.R., Griffin, D., Application of Rainbow Schlieren Deflectometry for Concentration Measurements in an Axisymmetric Helium Jet, Experiments in Fluids, 25-2, pp. 89-95, 1998.

[3] Kolhe, P.S. and Agrawal, A.K., Density Measurements in a Supersonic Microjet Using Miniature Rainbow Schlieren Deflectometry, *AIAA J.*, 47-4, pp. 830-838, 2009.

[4] Takano, H., Kamikihara, D., Ono, D., Nakao, S., Yamamoto, H., and Miyazato, Y., Three-Dimensional Rainbow Schlieren Measurements in Underexpanded Sonic Jets from Axisymmetric Convergent Nozzles, *J. Thermal Science*, 25-1, pp. 78-83, 2016.

[5] Zahiri, S.H., Yang, W., and Jahedi, M., Characterization of cold spray titanium supersonic jet, ASM International, 18-1, pp. 110-117, 2009.

[6] Foelsch, K., The analytical design of an axially symmetric Laval nozzle for a parallel and uniform Jet. J. Aeronautical Sciences, 16-3, pp. 161-166, and 188, 1949.

[7] Born, M. and Wolf, E., Principle of Optics, Pergamon Press, New York, p. 123, 1964.

[8] Agrawal, A. K., Butuku N. K., Gollahalli, S. R., and Griffin, D., Three-dimensional rainbow schlieren tomography of a temperature field in gas flows. *Applied Optics*, 37- 3, pp. 479-485, 1998.

[9] Honma, H., Ishihara, M., Yoshimura, T., Maeno, K., & Morioka, T., Interferometric CT measurement of three-dimensional flow phenomena on shock waves and vortices discharged from open ends. Shock Waves, 13, pp. 179-190, 2003.

[10] Faris G.W. & Byer, R. L., Three-dimensional beam-deflection optical tomography of a supersonic jet. *Applied Optics*, 27-24, pp. 5202-5212, 1988.

[11] Nakao, S., and Takamoto, M., Choking phenomena of sonic nozzles at low Reynolds numbers, *Flow Measurement and Instrumentation*, 11-4, pp. 285-291, 2000.

[12] Franquet E., Perrier V., GiboutI, S., and Brue, P., Free underexpanded jets in a quiescent medium: A review. *Progress in Aerospace Sciences*, 77, pp. 25-53, 2015.

[13] Panda, J., Shock oscillation in underexpanded screeching jets, *J. Fluid Mechanics*, 363, pp. 173-198, 1998.